Journal of Industrial and Engineering Chemistry 133 (2024) 219–227

Contents lists available at ScienceDirect

Journal of Industrial and Engineering Chemistry

journal homepage: www.elsevier.com/locate/jiec

Neutron imaging the spatial progression of chemical oxidation of lithium-ion cathode material in a packed bed reactor

Devanshi Gupta [a], Yuxuan Zhang [b], Ziyang Nie [a], Gary M. Koenig Jr. [a,*]

[a] Department of Chemical Engineering, University of Virginia, 102 Engineers' Way, P.O. Box 400741, Charlottesville, VA 22904 USA
[b] Neutron Scattering Division, Oak Ridge National Laboratory, P.O. Box 2008, Oak Ridge, TN 37831, USA

ARTICLE INFO

Keywords:
Chemical Redox
Redox targeting
Packed bed reactor
Lithium-Ion Materials
Delithiation

ABSTRACT

Emerging electrochemical systems relevant to energy applications including redox targeted flow batteries rely on chemical redox of solid electroactive materials using dissolved redox couples. One configuration to facilitate contact between the redox shuttles and solid material which is volume efficient is a packed bed reactor. While methods have been reported to assess the overall progression by analysis of the packed bed reactor effluent, herein analysis of the spatial progression of the chemical redox will be reported. Combination of neutron and x-ray tomography enabled assessing the pore and particle structure in the packed bed reactor and the spatial homogeneity of the reaction at different overall extents of conversion of the reactor bed. These characterization tools provide methods to probe the chemical redox processes occurring within the reactor environment.

Introduction

Chemical oxidation and reduction (e.g., redox) of solid electroactive material by dissolved electroactive species (redox shuttles) has emerged as a key process for multiple technologies. Perhaps the most well-known application where redox shuttles interact with solid electroactive particles has been overcharge protection, where electrochemical current was reported to be carried by dissolved species in the electrolyte to avoid reaching deleterious cell potentials [1,2]. In such processes, however, the redox shuttle was not necessarily targeted towards driving chemical redox of the solid phase material. A more direct example of chemical redox of solid electroactive material with redox shuttles have been redox-targeting flow batteries (RTFBs) [3,4]. In these systems, the majority of the energy was stored in solid particles within packed beds or tanks, and the power was delivered from redox shuttles which flowed through an electrochemical cell stack [5,6]. Extended discharge duration of the redox shuttles was enabled by the chemical redox process returning the shuttles to the "charged" state, and the chemical and electrochemical processes were reversible to enable large extents of oxidation and reduction of the shuttles and solid particles. Relative to conventional flow batteries that have both energy and power provided by dissolved electroactive species, solubility no longer limits energy density of RTFBs and thus they have been reported to potentially offer an increase in volumetric energy density by a factor of 8–10 over conventional flow batteries [3,4,7]. An intrinsic tradeoff for RTFBs relative to conventional flow batteries has been the need for a potential difference between the redox shuttles and the solid electroactive species to thermodynamically drive the chemical redox reactions, and thus round trip efficiency must be traded for the increased energy density. Another system which was similar in operation to RTFBs has also been reported for potentially recycling solutions from lithium-ion (Li-ion) battery electrodes [8]. In the recycling system, the redox shuttles and chemical redox were used to drive lithium in and out of a host solid electroactive material, with the goal of extracting and concentrating lithium ions to recycle the lithium from spent Li-ion battery cells.

The potential systems and applications of chemical redox of Li-ion solid electroactive material has led to recent research reports studying different aspects of the chemical and electrochemical processes involved. Experimental systems probing progression of the chemical redox process have included solid electroactive material in the form of dispersions, bound in composite electrode strips, and fused into sintered aggregates [6,7,9–11]. Many of these studies have been conducted in batch reactor configurations, which has advantages with regards to removing the additional complications of pumping systems and tubing and keeping total reactant amounts relatively low. However, batch setups make the use of larger amounts of electroactive material more challenging and from an RTFB application standpoint result in generally less loading/volume fraction of electroactive material, which reduces

* Corresponding author.
E-mail address: gary.koenig@virginia.edu (G.M. Koenig).

https://doi.org/10.1016/j.jiec.2023.11.060
Received 2 August 2023; Received in revised form 12 November 2023; Accepted 28 November 2023
Available online 30 November 2023

volumetric energy density of the system. To address these batch reactor limitations, packed bed reactors (PBRs) have been reported for analysis of chemical redox between redox shuttles and solid electroactive material [5,12]. For a PBR configuration, the electroactive particles have been loaded into a column, with the redox shuttle solution pumped through the column and reacting with the particle bed before exiting the column. Relative to alternatives such as a stirred tank reactor, a PBR can achieve more efficient electroactive material volume loading, which in principal will result in higher energy density when used in a RTFB application. A known drawback for a packed bed is the pressure drop for the fluid traversing the column which will require higher pumping energy. Another potential limitation of the PBR relative to batch configurations was that while most batch systems have been assumed to have the reaction uniformly distributed in space (e.g., well mixed), this assumption may not be valid for a PBR.

For many of the batch systems the reaction was assumed to be distributed uniformly, however; for systems with packed particles (including strips and pellets, and especially packed beds) the reaction progression and preferential flow path within the reaction zone containing particles has not been assessed. This is important for assessing homogeneity of particle utilization and the mechanism of the reaction (e.g., core–shell). As an example, heterogeneous reactions were studied inside a PBR at multiple scales using computational methods for CO_2 reduction to methanol[13], ethylene epoxidation[14], and methane dry reforming in spark plasma reactors[15]. Recently our group reported a PBR where the solid electroactive material was lithium iron phosphate ($LiFePO_4$, LFP) [12]. The LFP was packed into a column with a void fraction of 0.37. Chemical oxidation of the LFP proceeded via flowing an aqueous phase through the PBR that contained the redox shuttle potassium ferricyanide (FeCN). The overall reaction between LFP and FeCN was proposed as shown below:

$$LiFePO_4 + [Fe(CN)_6]^{3-} \rightarrow FePO_4 + [Fe(CN)_6]^{4-} + Li^+ \quad (1)$$

In this previous report, the impact of different parameters on conversion of LFP as a function of time (or equivalently redox shuttle solution volume) was investigated. The LFP conversion was determined via electrochemical analysis of the reactor effluent, where every mole of ferricyanide which was reduced in the effluent was assumed to correspond to a mole of LFP which was oxidized. However, even though the overall conversion of the LFP was inferred from the measured changes in the liquid effluent, no information was accessible on the homogeneity of the spatial variation for the LFP conversion. Accessing the spatial variation of the chemical oxidation of the LFP could provide insights into the limiting processes for the chemical conversion, and also whether the redox shuttle fluid can access all of the solid electroactive material within the column. For example, in the prior study it was not known whether there was radial and/or linear gradients and/or heterogeneity for the oxidation/delithiation of LFP, or whether particle size or pore size within the column influenced the preferential flow and reaction progression. As one extreme example, at an overall 50 % oxidation/delithiation of the LFP material in the PBR, this would correspond to either 50 % delithiation of all particles, or 100 % delithiation of only the particles in the top half (and 0 % delithiation of the bottom half). Distinguishing between these two extremes was not possible in the prior report, nor has access to such information in a redox targeted PBR been reported previously to the authors' knowledge.

Herein, we will describe an initial report of using neutron imaging to access the spatial distribution of chemical oxidation of LFP in a PBR. Neutron imaging has been previously reported as a non-destructive technique for accessing the spatial progression of *electrochemical* reactions in operando during charge and discharge of Li-ion batteries [16–21]. Neutron imaging was well suited to such characterization because of the interaction of the neutrons with light nuclei, especially Li, that greatly attenuate neutrons [18]. Thus, average transmission for neutrons incident on a sample was highly sensitive to Li^+ concentration, and because by far the most substantive change in composition during charge/discharge of Li-ion batteries was Li^+ concentration in the solid phase electroactive material within the electrodes, changes in neutron transmission during charge/discharge corresponded to the locations where electrochemical reactions occurred within the cell [19]. Thus, neutron imaging has provided information on spatial progression of electrochemical reactions within Li-ion cells. These prior results on electrochemical cells led us to hypothesize that neutron imaging could be used to assess the spatial distribution of the *chemical redox* process of oxidation of LFP with a redox shuttle (i.e., ferricyanide). In this initial demonstration of neutron imaging of a LFP packed bed which has undergone chemical oxidation with a redox shuttle flowed through the PBR, we conducted not just neutron imaging but also three-dimensional (3D) neutron tomography on the PBR. As will be described, tomography enabled probing semi-quantitatively the 3D heterogeneity of the chemical oxidation of LFP; however, due to the timescales required for collecting neutron tomography (~6–18 h) operando tomography experiments were not possible and analysis had to be conducted after the chemical oxidation process [18]. It is also noted that the resolution of the neutron tomography (pixel pitch for experiments herein of 43.4 μm) needed to be considered with regards to resolution of the reaction heterogeneity probed, however, the interstitial voids/pores and LFP aggregates were for the most part much larger than the pixel pitch. Particle aggregate and void size distributions relevant for this system were discussed in a prior report [12], and >99 % of the particle volume was particles with lengths over 0.5 mm and >75 % of the void volume was voids with widths >160 μm as determined from XCT analysis. Thus the technique still showed promise for the goal of tracking spatial reaction progression within the PBR.

Materials and methods

Columns were fabricated out of polytetrafluoroethylene (PTFE) and as received were 16 mm outer diameter (MSC). Columns were machined to have custom length of 10 mm and inner diameter of 10 mm. The PTFE columns were then filled with LFP (Xiamen TOB New Energy Technology, China) particles which had been sintered and then pulverized (see previous work for details on LFP processing [12]). LFP in the columns was supported by PTFE frits (Cole Parmer, 5 μm). Additional details on the PBR setup can be found in Supplementary Material.

A schematic for the PBR setup can be found in Fig. 1a. The FeCN solution was passed though the PBR with the driving force for flowing the solution provided by a syringe pump (KDS 100 Legacy). The Reynolds number for the packed bed was estimated to be 0.01, and thus within the laminar flow regime. Total reaction progression across the PBR was monitored using cyclic voltammetry (CV) analysis of aliquots collected from the reactor effluent (Fig. 1b). This technique for using CV to track the total progression of the chemical oxidation of the LFP by an FeCN redox shuttle was described in a previous study [12]. The relative amount of FeCN (Sigma Aldrich) in the oxidized form in the column effluent was determined from CV peak currents measured in the aliquots and by applying the Randles-Sevcik equation [22]. CV peak current was previously reported to have a linear dependence on FeCN relative fraction in the oxidized form using the same method [12]. The amount of FeCN in the effluent which had been reduced to Fe^{2+} was assumed to have gained an electron from chemical redox reaction with LFP (Eq. 1). Thus, the extent of overall LFP oxidation could be tracked for each aliquot which exited the column, consistent with previously reported and validated methods. Using electrochemical methods to track the progression of overall LFP oxidation in the column, it was possible to confirm nominally identical PBR experiments with regards to reaction progression were being conducted. For this report, the reaction was stopped at different extents of total LFP oxidation by stopping the redox shuttle feed to the reactor after a target conversion of the LFP material in the PBR to $FePO_4$ (FP). To stop the reaction, the feed was switched from the FeCN solution to water. This was accomplished by changing the feed

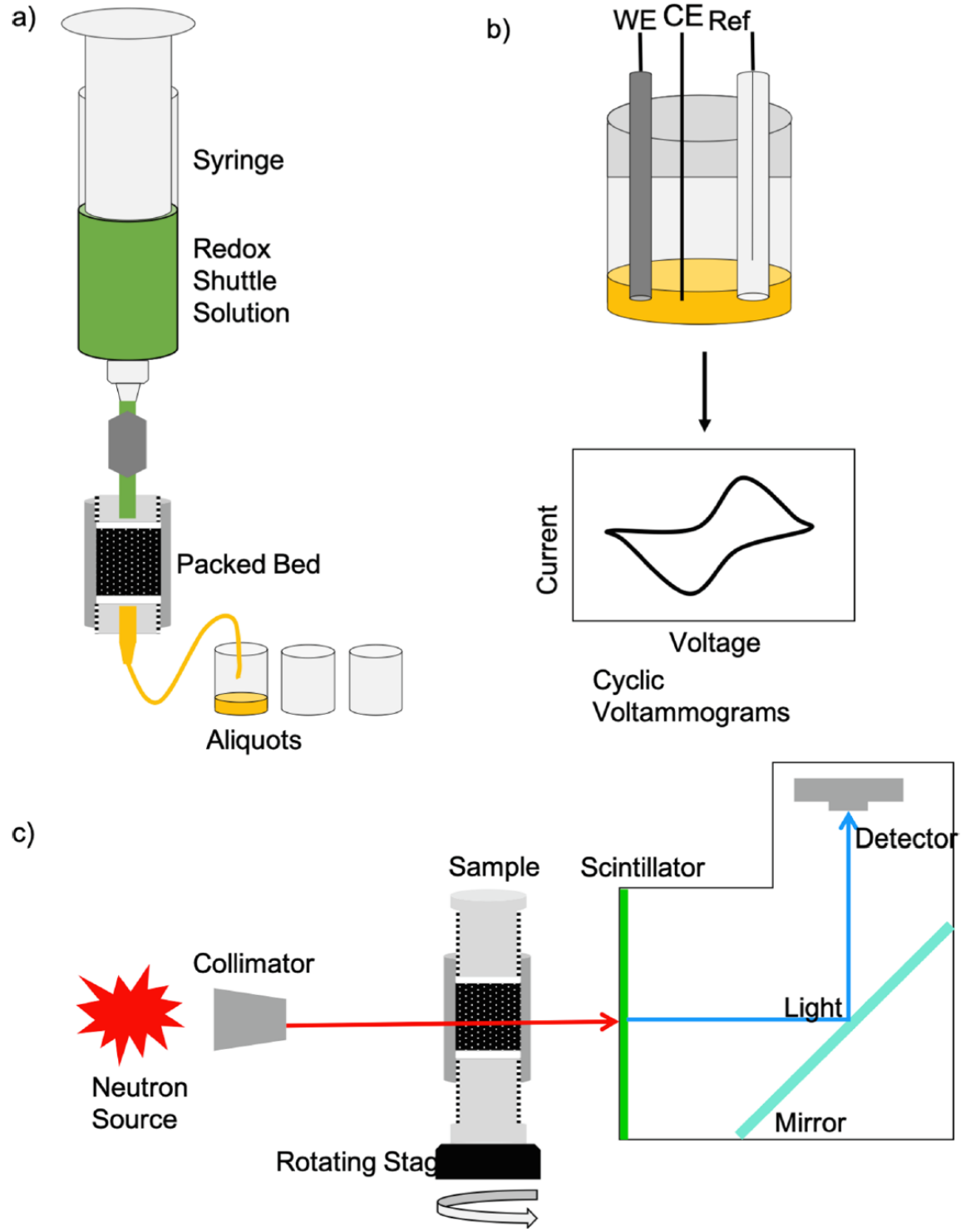

Fig. 1. Schematics of a) packed bed reactor experimental setup, b) three-electrode cells used for cyclic voltammetry on reactor effluent aliquots to determine overall reactor progression, and c) ex situ neutron imaging experimental setup at the CG-1D neutron imaging beamline at HFIR, ORNL. The objects are not drawn to scale and are for illustrative purposes only.

syringe from one containing the FeCN solution to one containing only water. A total of 50 mL of water was purged through the column, and CV analysis was conducted on aliquots during the purge to confirm that the features consistent with FeCN in solution was no longer detectable. Without additional FeCN fed, there was no longer an oxidizing agent to drive the LFP oxidation forward. In addition, as the water replaced the FeCN solution, it was expected that there were no longer sufficient ionic charge carriers to redistribute the lithium distribution between particles (including within porous aggregates) within the PBR. The water did not contain any salt (and thus no Li^+) and thus solution phase Li^+ transport was not expected to be able to redistribute Li^+. The water was also fed at the same temperature as the initial FeCN solution (i.e., room temperature). Thus, the total extent of reaction could be stopped at a targeted extent of LFP oxidation. The targeted amounts of LFP oxidation were approximately 25 %, 50 %, 75 %, and 100 %. For this study, a terminology of LFP-X was used, where X was the percentage of LFP in the PBR

(thus 100-X corresponded to the relative percentage of FP). As an example, LFP-75 contained 75 % LFP, which meant 25 % (on a molar basis) of the LFP had been oxidized to FP as determined from reactor effluent measurements.

In total, 5 samples were prepared. LFP-25, LFP-50, and LFP-75 were prepared by oxidizing LFP to the desired amount as described earlier via oxidation with FeCN. There was also a LFP-100 baseline which was packed with sintered LFP aggregates and never contacted any redox shuttle solution. A LFP-0 baseline had 100 % conversion of the LFP powder to FP. All samples which had been in contact with aqueous solutions were thoroughly dried via drying in a convection oven for 8 h at 80 °C and then vacuum oven for over 2 h at 120 °C.

Neutron imaging was conducted at the CG-1D neutron imaging beamline at the High Flux Isotope Reactor (HFIR) at Oak Ridge National Laboratory (ORNL)[23]. A cartoon schematic of the neutron imaging setup at CG-1D can be found in Fig. 1c. A collimated neutron source passed though the column, including the region that contained the LFP/FP packed bed of particles. The neutrons will interact with the entire PBR sample, and those that transmit through the sample will be converted into light signals at the scintillator screen. The light signal was reflected by a 45° mirror and recorded by a charge-coupled device (CCD) camera (Andor iKon-L 936). The sample column was mounted on a rotation stage that rotated from 0° to 360° during the computed tomography (CT) scan. At every 0.43°, a radiograph, called a projection, with 70 s exposure was collected. 2D projections were then reconstructed by iMars3D using filtered-back-projection [24].

X-ray computed tomography (XCT) was also conducted on the same LFP/FP PBR samples loaded into columns prior to the neutron computed tomography (NCT) experiments. Details of XCT setup can be found in a previous report [12]. Image processing and analysis of NCTs and XCTs were performed using Amira Avizo software packages. The experimental tomography images were analyzed in the context of the reactions occurring in the PBR and the packed material microstructure. This study reports for the first time the spatiotemporal variation of Li^+ distribution in the PBR designed towards RTFBs and other applications making use of chemical oxidation of solid electroactive materials.

Results

In this work, oxidation of LFP to FP in the PBR was expected to proceed according to the reaction in Eq. 1. As a result of this reaction, the net compositional change in the solid phase was loss of Li^+, with the loss of Li^+ corresponding to the extent to which the oxidation proceeded forward. This Li^+ was then carried away in the reactor effluent. Electrochemical analysis of the redox shuttles in the effluent was used to determine the overall conversion of the reactor, which enabled the different LFP-X compositional samples to be prepared. Due to the sensitivity of neutrons to lithium concentration, it was expected that the relative intensity of the neutron radiographs collected on the column samples would provide spatial information that corresponded to the relative lithium concentration (and thus relative extent of oxidation) of the LFP particles. Thus, neutron imaging was expected to provide visualization of how the chemical redox proceeded spatially in the packed bed. Neutron radiography measured the attenuation of the neutron beam resulting from the adsorption and scattering by the atoms in a sample of uniform thickness, as governed by Beer-Lambert-type behavior,

$$I(\lambda) = I_0 e^{-\mu \Delta x} \tag{2}$$

with incident intensity I_0 and transmitted intensity through the sample I. Δx is the thickness of the samples and μ is the attenuation coefficient given by,

$$\mu(\lambda) = \frac{\sigma_t(\rho N_A)}{M} \tag{3}$$

where σ_t is the cross-section for neutrons of the material with density ρ, N_A is Avogadro's number, and M is molar mass. Eq. (2) and (3) can be extended to heterogeneous and irregular thickness samples, such as those in this study, for neutron radiography and tomography.

Due to the fundamental nature of neutron interactions with materials as described by Eq. (2) and (3), and the high attenuation by lithium, neutron imaging has previously shown great sensitivity to the Li^+ composition for LFP [18]. In Fig. 2a, two-dimensional neutron radiographs of the five LFP-X column samples with different degrees of delithiation from chemical oxidation are shown. The fluid flow during the reaction process was from top to bottom in the images, which was also in the same direction as the force of gravity. The mean neutron transmission from the radiographs was then normalized for the cylindrical sample geometry, and the mean transmission through the region of the columns packed with LFP/FP particles was determined. This mean neutron transmission (relative to average transmission of neutrons determined from the mean neutron transmission from regions of the detector that did not contain any sample material the neutrons passed though) can be found in Fig. 2b. It was found that there was a linear relationship between total Li^+ concentration of the solid material loaded in the column and the average neutron transmission (R^2 = 95.6 %), where LFP-100 had the lowest average relative transmission and LFP-0 had the highest average neutron transmission. This outcome was consistent with the expectation that samples with higher Li concentration would have higher neutron attenuation and thus lower neutron transmission. While the average neutron transmission across the column regions loaded with particles was consistent with the overall Li^+ concentration progression, regions of heterogeneity with regards to neutron radiograph contrast/intensity were noted. As one example, there was a noticeable region on the right-hand side of LFP-25 which was darker than the rest of the sample. This result suggested that corresponding region likely had a relatively higher Li^+ concentration, suggesting that there were regions within the column that had experienced much less oxidation/delithiation during the chemical redox process. To gain further insights into the heterogeneity of the chemical oxidation and preferential flow path within the column, neutron tomography was also assessed for the column samples and will be discussed in further detail below (NCT cross-sections can be found in Fig. 3a–e and Fig. 4a–c.

Fig. 3 contains radial cross-sections extracted from NCTs (Fig. 3a–e) or XCTs (Fig. 3f–j) for the different LFP-X materials. NCTs were complemented with XCTs in part because XCT had a smaller pixel pitch of 16 μm to gain further insights to pore/void and particle size impacts to the delithiation of LFP in the PBR [16,25]. NCT has successfully been used to study Li-ion diffusion, gas evolution, and electrolyte consumption [26–31]. However, recently LaManna et al [32], Zieshe et al. [16], and Tengattini et al. [33] have demonstrated the combined use of XCT and NCT, which can provide additional insights into the materials being imaged. Radiographs were extracted from the XCT and NCT images at the approximate midway location of the packed bed height, and while collected at separate times and on separate instruments the radiographs have been aligned to correspond to the same regions in the sample.

For the neutron radiographs extracted from NCTs in Fig. 3a-e, the average attenuation of the neutrons that passed through the PBR was represented by the indicated prismatic color scheme, with bright reds and oranges correlating to regions of high attenuation coefficient (mm^{-1}) and blues and violets corresponding to regions of relatively low neutron attenuation coefficient. Li was the highest attenuating element in the PBR, and thus the high attenuation regions were expected to correspond to high Li concentration regions and low attenuation regions were expected to correspond to low Li concentration regions. While LFP-100 (Fig. 3a) had many regions of yellow and red which corresponded to high attenuation/Li concentration, the LFP-0 (Fig. 3e) was almost all blue which corresponded to low attenuation/Li concentration. This result would be expected due to the dramatic differences in Li content in the LFP solid phase for the 2 samples of 8.07 mol/L for LFP-100 and ~0

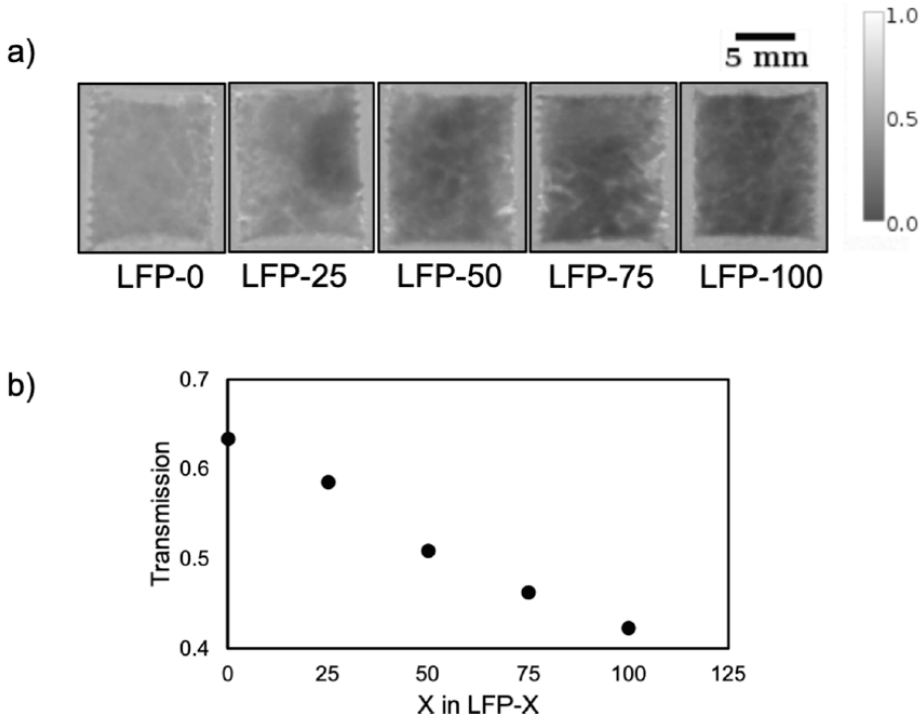

Fig. 2. a) Normalized radiographs of LFP/FP packed bed reactors at the five different extents of reaction/delithiation of the LFP assessed in this study. Color scale corresponds to relative transmission in image using grayscale. b) Mean relative transmission (95 % confidence intervals for ~70,000 pixels, where interval was smaller than data point height) of neutrons through the packed bed region as a function of the overall relative LFP amount (balance was FP) in the packed bed reactor. Fluid flow direction for images in a) was from top to bottom.

mol/L for LFP-0. LFP-75 (Fig. 3b), LFP-50 (Fig. 3c), and LFP-25 (Fig. 3d) were intermediate relative to the LFP-100 and LFP-0 concentration endpoints; however, it was noted that these intermediate samples had much more heterogeneity in the attenuation/Li distribution. When comparing the neutron and x-ray images side-by-side, it was generally observed that higher attenuation occurred in the larger aggregates, and that for samples with increasing delithiation there was higher attenuation towards the center of the particle aggregates compared to the surface of the aggregates. This observation would be consistent with the delithiation/oxidation propagating into the aggregate interior as the reaction progressed, suggesting that the reaction rate may have been limited by liquid phase microstructure transport of the redox shuttles to the aggregate interiors. Given the many orders of magnitude lower diffusion coefficient for Li^+ in the solid LFP/FP compared to FeCN or Li^+ in the aqueous phase, it was not expected that solid phase transport contributed substantially to the Li^+ redistribution within the particle aggregates or column. There was also attenuation heterogeneity observed that was much larger length scale than the particle aggregates. For example, the lower left region of LFP-25 was almost all low attenuation (Fig. 3d), even though there were a number of larger aggregates within that corresponding region as seen in the x-ray image (Fig. 3i). This outcome was speculated to have resulted from the bulk electrolyte flow and better access to the low attenuation regions (to proceed with oxidation/delithiation) compared to the high attenuation regions. This speculation will be further discussed below.

Fig. 4 displays axial cross-sections for the PBR for LFP-75, LFP-50, and LFP-25. The three intermediate extents of delithiation were chosen because at 0 % (e.g., LFP-100) and 100 % (e.g., LFP-0) oxidation/delithiation heterogeneity in attenuation for the different larger regions containing particle aggregates in the bed would not be expected and was not observed. The cross-sections were either neutron images extracted from NCT (Fig. 4a–c), x-ray radiographs extracted from XCT (Fig. 4d–f), or pore distance maps determined from analysis of the XCT data (Fig. 4g–i). For each sample, the images have been aligned to correspond to the same sample regions. At 25 % delithiation (LFP-75, Fig. 4a), smaller-sized particles from the XCT-extracted image appeared to correspond to lower attenuation and greater delithiation relative to larger particle aggregates in the NCT-extracted image. This outcome was consistent with observations on the radial images (Fig. 3) and with transport limitations in the microstructure of the LFP aggregates limiting the reaction progression due to mass transport accessibility to the interiors of the larger aggregates. It was also noted that there was lower attenuation and thus greater extent of oxidation for regions corresponding to the top of the PBR relative to the bottom. The redox shuttle solution progressed downward from the top of the column to the bottom, and thus the greater extent of delithiation at the top may have been a consequence of those regions first contacting the redox shuttle solution, where the relative concentration of the reactive Fe^{3+} form of the redox shuttle would be the greatest.

For LFP-50 and LFP-25, there were notable regions of attenuation heterogeneity in the neutron images (Fig. 4b, c). For example, the region on the right-hand side of the column for LFP-50 had much lower attenuation, suggesting much greater extents of delithiation and oxidation. It was noted that this area had relatively higher extents of delithiation even though it corresponded to relatively large LFP aggregates. It is speculated that the heterogeneity in delithiation of the LFP may have been due to access of the redox shuttle solution following the preferential flow path to the different regions of the column. Additional analysis to support this limitation can be found in Fig. 4h, which contains maps of pore lengths extracted from the XCT images. When comparing Fig. 4b and h, it can be seen that regions of the column with large extents of delithiation also corresponded to regions with larger pores that were more interconnected. A region on the left-hand side with the relatively smallest pore lengths also corresponded to the highest attenuation/lowest delithiation region in the column. It was suspected that the larger and connected pore regions facilitated lower resistance to bulk fluid flow, and that the redox shuttle solution preferentially accessed these regions of the column. This concept was also supported

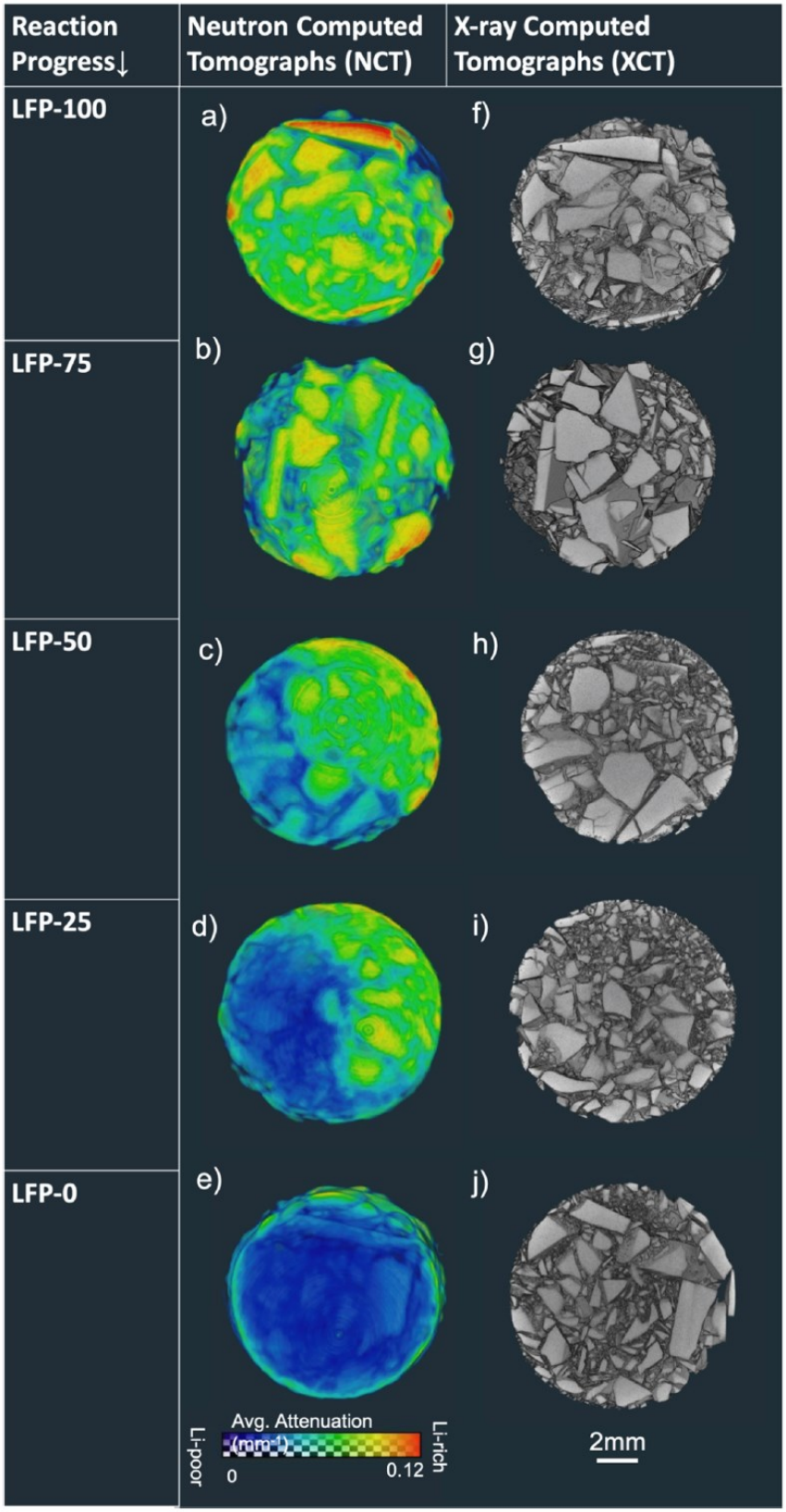

Fig. 3. Extracted radial cross-sections of the LFP/FP packed bed reactor from 3D reconstructed NCTs (left) and XCTs (right). On the left, (a-e) average attenuation (mm^{-1}) of neutron beam is represented by the contrast between the particles (refer to color scale on the left). On the right (f-j), aligned XCT images show LFP aggregates and pore/void regions. Each row corresponds to a different overall LFP/FP extent of lithiation (e.g., LFP-X).

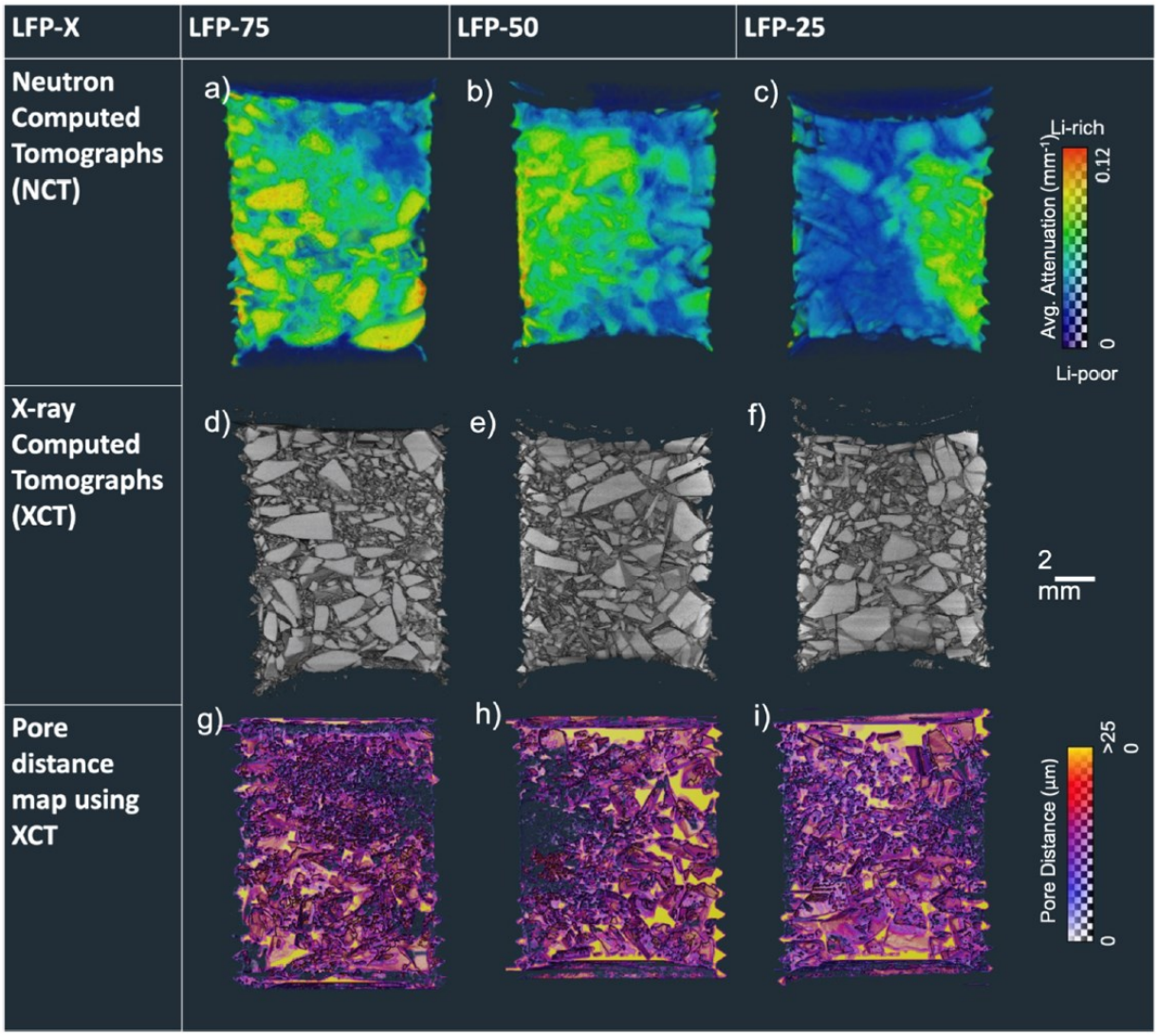

Fig. 4. Extracted cross-sections along the length of the LFP/FP packed bed reactor from 3D reconstructed NCTs (a-c) and XCTs (d-f) in the same corresponding regions aligned to match for each sample (LFP-75, LFP-50, and LFP-25). The bottom row (g-i) contains pore distance maps extracted from analysis of the corresponding XCT data. The color scales for top and bottom row represent average attenuation (mm^{-1}) of the neutron beam, and the distance between pores, respectively. Fluid flow direction for all images was from top to bottom.

by the neutron images and pore length analysis from XCT that can be found for LFP-25 in Fig. 4c and i, respectively. The region with the smallest pore lengths on the right hand side also had the relatively highest attenuation and the relatively lowest extent of oxidation/delithiation, consistent with the redox shuttle fluid restricted from accessing this region.

Discussion

The results above provide insights into the internal reaction progression of a LFP PBR. Such a reactor is relevant to applications including RTFBs and Li-ion material recycling. While overall effluent concentration measurements using electrochemical methods were previously reported to capture average reaction extent for the electroactive powder in a PBR [12], radiographs extracted from NCTs and XCTs on the packed bed region after different extents of reaction suggested that the aggregate size and fluid accessibility were both important to oxidation of the LFP aggregates. It is noted here that the NCT and XCT characterization was all ex situ on extracted columns, and better access to the dynamics of the reaction progression could be obtained by in operando neutron imaging on the packed bed. Monitoring the reaction progression in real time will likely be limited to 2D projections of the column rather than 3D NCT due to the dramatically different timescales for 2D and 3D neutron imaging collection.

The results of this study also suggested that particle morphology and pore connectivity play key roles in the preferential flow path and resulting heterogeneity of the reaction progression. It is suggested that future studies with electroactive particle aggregates of more uniform size and shape will enable less ambiguous verification of whether the rate limiting process is liquid phase redox shuttle transport through the particle aggregate microstructure. Pore connectivity can be more difficult to control, but by varying particle size, shape, and/or loading different pore sizes and connections should be attainable. Detailed study of the mass transport processes within the PBR will provide insights into the overall operation and limitations of the larger scale systems such as RTFBs with PBRs.

Conclusions

LFP solid electroactive materials were packed into a column and oxidized via a chemical redox process using dissolved redox shuttles to different extents of overall oxidation as determined by analysis of the

reactor effluent. Neutron imaging was conducted on the packed bed reactors containing the LFP materials that had different extents of oxidation. Changes in the average attenuation of the neutrons as a function of the chemical oxidation progression for the overall packed bed volume was consistent with expectations based on the net overall expected change in lithium concentration in the packed bed. Neutron tomography on the packed bed samples indicated that the reaction distribution across the reactor was not homogeneous, with larger particle aggregates generally retaining more attenuation and regions with finer pores/voids and less pore connectivity also maintaining relatively higher attenuation. These results support that neutron imaging can be used as a tool to track the spatial progression of chemical redox processes where there are net changes in lithium composition, and that the particle organization and microstructure influence the spatial homogeneity of the redox reaction. It is noted that for the packed bed reactor some heterogeneity is expected to be unavoidable, for example gradients in the LFP oxidation as a function of column length. However, within more local regions of the column it would be desirable to avoid the zones of lower extent of reaction caused by restricted access of the electrolyte. It is expected low activity regions will reduce utilization of the reactor. Analysis of the spatial distribution of chemical redox of lithium-ion battery electroactive materials will be important in the design and optimization of applications that take advantage of these processes, such as redox targeting flow batteries.

Declaration of competing interest

The authors declare that they have no known competing financial interests or personal relationships that could have appeared to influence the work reported in this paper.

Acknowledgements

This research was funded by the National Science Foundation, award number 1940915. Part of this research used resources at the High Flux Isotope Reactor, a DOE Office of Science User Facility operated by Oak Ridge National Laboratory. A co-author on this manuscript is at UT-Battelle, LLC, under contract DE-AC05-00OR22725 with the US Department of Energy (DOE). The US government retains and the publisher, by accepting the article for publication, acknowledges that the US government retains a nonexclusive, paid-up, irrevocable, worldwide license to publish or reproduce the published form of this manuscript, or allow others to do so, for US government purposes. DOE will provide public access to these results of federally sponsored research in accordance with the DOE Public Access Plan.

Appendix A. Supplementary material

Supplementary data to this article can be found online at https://doi.org/10.1016/j.jiec.2023.11.060.

References

[1] L. Zhang, Z. Zhang, K. Amine, Redox Shuttle Additives for Lithium-Ion Battery. In: Lithium Ion Batteries - New Developments, 2012. https://doi.org/10.5772/26572.
[2] J. Chen, C. Buhrmester, J.R. Dahn, Chemical overcharge and overdischarge protection for lithium-ion batteries, Electrochem Solid-State Lett. 8 (1) (2005) A59, https://doi.org/10.1149/1.1836119.
[3] Q. Huang, H. Li, M. Grätzel, Q. Wang, Reversible chemical delithiation/lithiation of $LiFePO_4$: towards a redox flow lithium-ion battery, Phys. Chem. Chem. Phys. 15 (6) (2013) 1793–1797, https://doi.org/10.1039/c2cp44466f.
[4] R. Yan, Q. Wang, Redox-targeting-based flow batteries for large-scale energy storage, Adv Mater. 1802406 (2018) 1802406, https://doi.org/10.1002/adma.201802406.
[5] L. Fan, C. Jia, Y.G. Zhu, Q. Wang, Redox targeting of prussian blue: Toward low-cost and high energy density redox flow battery and solar rechargeable battery, ACS Energy Lett. 2 (3) (2017) 615–621, https://doi.org/10.1021/acsenergylett.6b00667.
[6] C. Jia, F. Pan, Y.G. Zhu, Q. Huang, L. Lu, Q. Wang, High – energy density nonaqueous all redox flow lithium battery enabled with a polymeric membrane, Sci. Adv. 1 (10) (2015) 1–7, https://doi.org/10.1126/sciadv.1500886.
[7] J.F. Vivo-Vilches, A. Nadeina, N. Rahbani, V. Seznec, D. Larcher, E. Baudrin, $LiFePO_4$-ferri/ferrocyanide redox targeting aqueous posolyte: Set-up, efficiency and kinetics, J. Power Sources 2021 (488) (2020), 229387, https://doi.org/10.1016/j.jpowsour.2020.229387.
[8] J. Yu, X. Wang, M. Zhou, Q. Wang, A redox targeting-based material recycling strategy for spent lithium ion batteries, Energy Environ. Sci. 12 (9) (2019) 2672–2677, https://doi.org/10.1039/c9ee01478k.
[9] F. Pan, J. Yang, Q. Huang, X. Wang, H. Huang, Q. Wang, Redox targeting of anatase TiO_2 for redox flow lithium-ion batteries, Adv Energy Mater. (2014), https://doi.org/10.1002/aenm.201400567.
[10] D. Gupta, G.M. Koenig, Analysis of chemical and electrochemical lithiation/delithiation of a lithium-ion cathode material, J. Electrochem. Soc. 167 (2) (2020), 020537, https://doi.org/10.1149/1945-7111/ab6bbf.
[11] D. Gupta, C. Cai, G.M. Koenig, Comparative analysis of chemical redox between redox shuttles and a lithium-ion cathode material via electrochemical analysis of redox shuttle conversion, J. Electrochem. Soc. 168 (5) (2021), 050546, https://doi.org/10.1149/1945-7111/ac0068.
[12] D. Gupta, Y. Zhang, Z. Nie, J. Wang, G.M. Koenig, Chemical redox of lithium-ion solid electroactive material in a packed bed flow reactor, Chem. Eng. Sci. 251 (2022), 117443, https://doi.org/10.1016/j.ces.2022.117443.
[13] A. Pavlišič, M. Huš, A. Prašnikar, B. Likozar, Multiscale modelling of CO_2 reduction to methanol over industrial $Cu/ZnO/Al_2O_3$ heterogeneous catalyst: linking ab initio surface reaction kinetics with reactor fluid dynamics, J. Clean Prod. (2020) 275, https://doi.org/10.1016/j.jclepro.2020.122958.
[14] M. Huš, M. Grilc, A. Pavlišič, B. Likozar, A. Hellman, Multiscale modelling from quantum level to reactor scale: an example of ethylene epoxidation on silver catalysts, Catal. Today. 2019 (338) (2018) 128–140, https://doi.org/10.1016/j.cattod.2019.05.022.
[15] D. Lašič Jurković, J.L. Liu, A. Pohar, B. Likozar, Methane dry reforming over Ni/Al_2O_3 catalyst in spark plasma reactor: linking Computational Fluid Dynamics (CFD) with reaction kinetic modelling, Catal. Today. 2021 (362) (May 2020) 11–21, https://doi.org/10.1016/j.cattod.2020.05.028.
[16] R.F. Ziesche, T. Arlt, D.P. Finegan, et al., 4D imaging of lithium-batteries using correlative neutron and X-ray tomography with a virtual unrolling technique, Nat. Commun. 11 (1) (2020) 1–11, https://doi.org/10.1038/s41467-019-13943-3.
[17] Z. Nie, R. Parai, C. Cai, C. Michaelis, J.M. LaManna, D.S. Hussey, D.L. Jacobson, D. Ghosh, G.M. Koenig, Pore microstructure impacts on lithium ion transport and rate capability of thick sintered electrodes, J. Electrochem. Soc. 168 (6) (2021), 060550, https://doi.org/10.1149/1945-7111/ac0bf6.
[18] Z. Nie, P. McCormack, H.Z. Bilheux, J.C. Bilheux, J.P. Robinson, J. Nanda, G. M. Koenig Jr, Probing lithiation and delithiation of thick sintered lithium-ion battery electrodes with neutron imaging, J. Power Sources. 419 (January) (2019) 127–136, https://doi.org/10.1016/j.jpowsour.2019.02.075.
[19] Z. Nie, S. Ong, D.S. Hussey, J.M. Lamanna, D.L. Jacobson, G.M. Koenig, Probing transport limitations in thick sintered battery electrodes with neutron imaging, Mol. Syst. Des. Eng. 5 (1) (2020) 245–256, https://doi.org/10.1039/c9me00084d.
[20] C. Cai, Z. Nie, J.P. Robinson, D.S. Hussey, J.M. LaManna, D.L. Jacobson, G. M. Koenig, Thick sintered electrode lithium-ion battery discharge simulations: incorporating lithiation-dependent electronic conductivity and lithiation gradient due to charge cycle, J. Electrochem. Soc. 167 (14) (2020), 140542, https://doi.org/10.1149/1945-7111/abc747.
[21] H. Zhou, K. An, S. Allu, et al., Probing multiscale transport and inhomogeneity in a lithium-ion pouch cell using in situ neutron methods, ACS Energy Lett. 1 (5) (2016) 981–986, https://doi.org/10.1021/acsenergylett.6b00353.
[22] J.E. Baur, R.M. Wightman, Diffusion coefficients determined with microelectrodes, J. Electroanal. Chem. 305 (1) (1991) 73–81, https://doi.org/10.1016/0022-0728(91)85203-2.
[23] L. Santodonato, H. Bilheux, B. Bailey, S. Pannala, J. Li, H.Z. Bilheux, S.K. Martha, J. Nanda, The CG-1D neutron imaging beamline at the Oak Ridge National Laboratory high flux isotope reactor, Phys Procedia. 2015 (69) (2014) 104–108, https://doi.org/10.1016/j.phpro.2015.07.015.
[24] https://imars3d.readthedocs.io/en/latest/.
[25] J.M. LaManna, D.S. Hussey, E.M. Baltic, D.L. Jacobson, Improving material identification by combining x-ray and neutron tomography. 2017;1039104 (September 2017):3. https://doi.org/10.1117/12.2274443.
[26] G.V. Riley, D.S. Hussey, D. Jacobson, In situ neutron imaging of alkaline and lithium batteries, ECS Trans. 25 (35) (2010) 75–83, https://doi.org/10.1149/1.3414005.
[27] J.B. Siegel, X. Lin, A.G. Stefanopoulou, D. Gorsich, Neutron imaging of lithium concentration in battery pouch cells, Proc. Am. Control Conf. (2011:) 376–381, https://doi.org/10.1109/acc.2011.5990883.
[28] J.B. Siegel, A.G. Stefanopoulou, P. Hagans, Y. Ding, D. Gorsich, Expansion of lithium ion pouch cell batteries: observations from neutron imaging, J. Electrochem Soc. 160 (8) (2013) A1031–A1038, https://doi.org/10.1149/2.011308jes.
[29] B. Michalak, B.B. Berkes, H. Sommer, T. Bergfeldt, T. Brezesinski, J. Janek, Gas evolution in $LiNi_{0.5}Mn_{1.5}O_4$/Graphite cells studied in operando by a combination of differential electrochemical mass spectrometry, neutron imaging, and pressure measurements, Anal Chem. 88 (5) (2016) 2877–2883, https://doi.org/10.1021/acs.analchem.5b04696.
[30] D. Goers, M. Holzapfel, W. Scheifele, E. Lehmann, P. Vontobel, P. Novák, In situ neutron radiography of lithium-ion batteries: The gas evolution on graphite

electrodes during the charging, J. Power Sources 130 (1–2) (2004) 221–226, https://doi.org/10.1016/j.jpowsour.2003.11.065.
[31] N. Kardjilov, A. Hilger, I. Manke, M. Strobl, W. Treimer, J. Banhart, Industrial applications at the new cold neutron radiography and tomography facility of the HMI, Nucl. Instruments Methods Phys. Res. Sect A Accel. Spectrometers, Detect Assoc Equip. 542 (1–3) (2005) 16–21, https://doi.org/10.1016/j.nima.2005.01.005.
[32] J.M. LaManna, D.S. Hussey, E.M. Baltic, D.L. Jacobson, Improving material identification by combining x-ray and neutron tomography. In: B. Müller, G. Wang (Eds.) Developments in X-Ray Tomography XI. SPIE; 2017:3. https://doi.org/10.1117/12.2274443.
[33] A. Tengattini, N. Lenoir, E. Andò, B. Giroud, D. Atkins, J. Beaucour, G. Viggiani, NeXT-Grenoble, the Neutron and X-ray tomograph in Grenoble, Nucl. Instruments Methods Phys. Res. Sect A Accel. Spectrometers, Detect Assoc. Equip. 968 (April) (2020), 163939, https://doi.org/10.1016/j.nima.2020.163939.